Acoustic spin-dependent topological bound states in the continuum with antihelical transport

Yuanshuo Liu,[1,*] Haonan Wang,[1,*] Hui Liu,[1,†] Pengtao Lai,[1] Yugan Tang,[1] Hua Cheng,[1,‡] and Shuqi Chen[1,2,3,§]

[1]*The Key Laboratory of Weak Light Nonlinear Photonics, Ministry of Education, School of Physics and TEDA Institute of Applied Physics, Nankai University, Tianjin 300071, China*

[2]*School of Materials Science and Engineering, Nankai University, Tianjin 300350, China*

[3]*The Collaborative Innovation Center of Extreme Optics, Shanxi University, Taiyuan, Shanxi 030006, China*

(Received 30 October 2025; revised 16 January 2026; accepted 28 January 2026; published 17 February 2026)

Bound states in the continuum (BICs) are spatially confined modes that coexist within the continuous spectrum propagating in the medium. The combination with topological physics gives rise to the topological BICs, which inherit the characteristics of traditional BICs and also have the features of topological protection. Here, we report the spin-dependent topological BICs that can support antihelical edge transport modes in a phononic crystal. We employ two decoupled spin subspaces as a bridge to topological BICs, which not only enable the spin-dependent topological BICs but also exhibit novel transport properties, antihelical edge transport. We experimentally realize the spin-dependent topological BICs in a phononic crystal and observe their hallmark, antihelical edge states embedded in the bulk structure with opposite spin. Furthermore, by tuning the interlayer coupling strengths, we experimentally achieve the independent modulation of the two topological BICs with different spins, giving rise to a hybrid system where spin-dependent topological BICs and topological flat bands coexist. Our work deepens the understanding of constructing topological BICs via spin subspaces and opens new avenues for hybrid multimode transport.

DOI: 10.1103/gmbp-csmg

I. INTRODUCTION

Bound states in the continuum (BICs) represent a counterintuitive class of wave-localized phenomena, where spatially confined modes coexist within the continuous spectrum of extended states [1,2]. Since the advent of quantum mechanics, BICs have been experimentally realized in a variety of wave systems, including electromagnetic [3–12], acoustic [13–17], and water waves [18,19]. The underlying mechanisms of forming BICs are diverse, encompassing symmetry incompatibility [3], separation of coordinate variables [4], parameter tuning [5–7,13–15], and inverse construction [8,9,18]. Owing to their high-Q factors and strong field confinement, BICs have found widespread applications in emerging photonic devices including ultrasensitive sensors [20] and low-threshold lasers [10–12]. Topological edge states, serving as ideal localized transport states, exhibit exceptional capabilities for wave manipulation and extraordinary robustness against disorder and defects [21–23]. Since the discovery of the first topological states characterized by the Z topological invariant in condensed matter systems [24], topological states have long been fanatically pursued as ideal transport states. The introduction of spin as a new degree of freedom gives rise to another class of topological phases characterized by the Z_2 topological invariant, which do not require time-reversal symmetry breaking [25,26]. With the development of artificial gauge fields, spin, as an important role in topological physics, enriches novel topological phases while also offers enhanced control of wave field transmission. A paradigmatic example is spin Chern insulator [27–30], which supports helical edge transport modes with 'spin-momentum locking'. Different spin states propagate in opposite directions along two parallel boundaries of the system, forming two spin-dependent transport channels. Recently, antihelical edge states [31–35], in stark contrast to helical edge modes, have attracted widespread attention. They support waves with the same spin polarization propagating in the same direction along two parallel boundaries, thereby enabling exceptional spin-dependent manipulation that overcomes the transmission direction limitations of traditional helical modes. To date, topological phases have exerted a profound impact on various research fields, owing to their extraordinary robustness and capacity for wave field manipulation.

The recent integration of topological theory [21–23] with BICs has given rise to topological BICs [36–45]. In these novel systems, nontrivial topological edge states can spectrally overlap with the bulk continuum while remaining mutually nonhybridized. Unlike conventional BICs that are easily destroyed by perturbations such as parameter variations or sample defects [2,3], topological BICs exhibit exceptional robustness to disorder and defects due to topological protection. A universal strategy, such as mirror stacking [39], introduces subspaces with opposite mirror parity by constructing bilayer structures, thereby converting nontrivial bound states in the original monolayer into topological BICs. Similar strategies have yielded a variety of novel topological BICs, such as higher-order topological BICs [40–42], valley states as topological BICs [43,44], and non-Abelian topological

*These authors contributed equally to this work.
†Contact author: hliu@nankai.edu.cn
‡Contact author: hcheng@nankai.edu.cn
§Contact author: schen@nankai.edu.cn

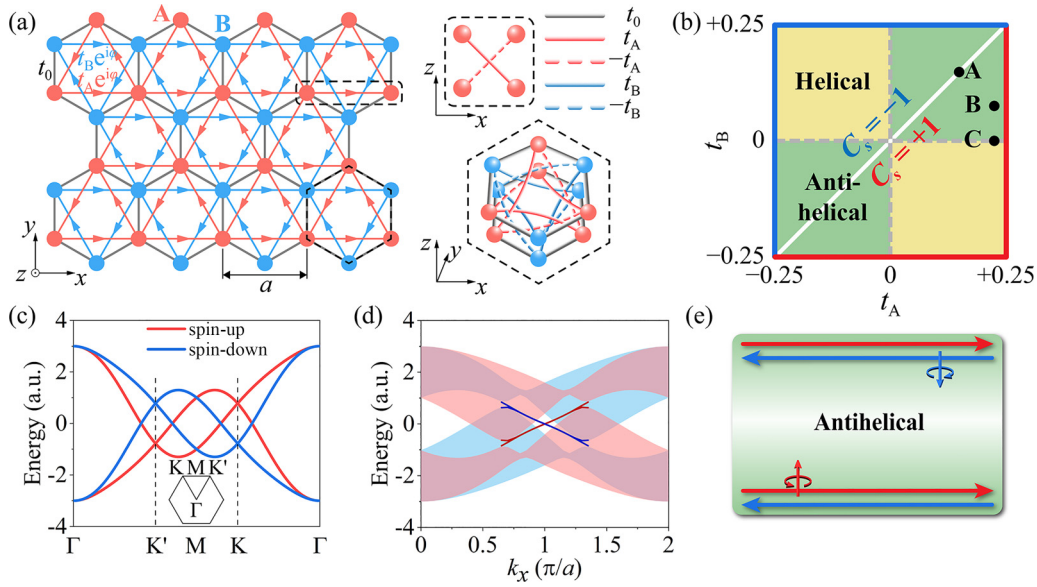

FIG. 1. Tight-binding model. (a) Schematic of the modified Kane-Mele model schematic. The rectangular dashed box highlights the interlayer coupling scheme, while the hexagonal dashed box outlines the unit cell. (b) Topological phase diagram in the parameter space of (t_A, t_B), revealing distinct edge-state distributions and spin-Chern number domains. (c) Bulk band structure calculated at point A in (b). (d) Projected dispersions for a strip with zigzag edges. Spin-up (spin-down) polarized edge-state dispersions are denoted by red (blue) lines, and the corresponding bulk-projected dispersions are indicated by light red (light blue) shaded regions. (e) Transport schematic of antihelical edge states, where identically spin-polarized edge states propagate in the same direction along two parallel zigzag edges.

BICs [45], yet they inevitably introduce additional system complexity. To date, these works on topological BICs have not involved the spin degree of freedom. In fact, decoupled spin spaces, serving as a natural condition for constructing BICs and topological phases, hold great potential for fully utilizing the subspaces and significantly enriching the degrees of freedom of topological BICs.

In this work, we propose spin-dependent topological BICs with antihelical edge transport in a phononic crystal. Taking spin as a natural framework, we construct a pair of spin-dependent topological BICs, where spin-dependent bulk and antihelical edge modes exhibit spectral overlap without hybridization. Meanwhile, we confirm that the novel propagation of the antihelical edge states is preserved that support the propagation of waves with the same spin polarization in the same direction along two parallel boundaries, despite being embedded in the bulk mode. In addition, by tuning the interlayer coupling strengths between sublattices, we can achieve independent control over the group velocity of antihelical edge transport in the topological BICs, thereby giving rise to a hybrid system where spin-dependent topological BICs and topological flat bands coexist. Both theoretical findings and experimental results offer robust evidence in support of these new phenomena. Our work not only provides further insight into the spin-dependent topological physics and topological BICs, but also establishes a new paradigm for high-efficiency multimode hybrid transport.

II. MODEL AND METHODS

We start with a lattice of the modified Kane-Mele model, shown in the left panel of Fig. 1(a), which comprises sublattices A and B indicated by red and blue dots, respectively. It features real-valued nearest-neighbor coupling t_0 and sublattice-dependent next-nearest-neighbor couplings $t_A e^{i\varphi}$ and $t_B e^{i\varphi}$, generating staggered effective magnetic fluxes. A physically implementable scheme for realizing such fluxes is to transform the system into a bilayer model with staggered positive and negative interlayer couplings, as indicated by the dashed rectangular frame in the right panel of Fig. 1(a). For simplicity, we set the intralayer coupling strength to $t_0 = 1$ (gray lines), while assigning the interlayer coupling strength of sublattices A and B as $\pm t_A$ (red lines) and $\pm t_B$ (blue lines), respectively. This configuration yields the unit cell highlighted by the hexagonal dashed box. The bilayer structure provides a layer degree of freedom, denoted by $\uparrow/\downarrow$ for the upper/lower layer. In the basis of $(A_\uparrow, B_\uparrow, A_\downarrow, B_\downarrow)^{\mathrm{T}}$, the tight-binding Hamiltonian $H(\mathbf{k})$ of the unit cell can be written as

$$H(\mathbf{k}) = \begin{pmatrix} 0 & h_{12} & \mathrm{i}h_{13} & 0 \\ h_{12}^* & 0 & 0 & \mathrm{i}h_{24} \\ -\mathrm{i}h_{13}^* & 0 & 0 & h_{34} \\ 0 & -\mathrm{i}h_{24}^* & h_{34}^* & 0 \end{pmatrix}, \tag{1}$$

where $h_{12} = h_{34} = t_0(e^{-\frac{\mathrm{i}k_y a}{\sqrt{3}}} + 2\cos(\frac{k_x a}{2})e^{\frac{\mathrm{i}k_y a}{2\sqrt{3}}})$, $h_{13} = 2t_A(2\sin(\frac{k_x a}{2})\cos(\frac{\sqrt{3}k_y a}{2}) - \sin k_x a)$, and $h_{24} = 2t_B(2\sin(\frac{k_x a}{2})\cos(\frac{\sqrt{3}k_y a}{2}) - \sin k_x a)$. Through a unitary transformation $U = \frac{1}{\sqrt{2}}\begin{pmatrix} 1 & \mathrm{i} \\ 1 & -\mathrm{i} \end{pmatrix} \otimes \mathrm{I}_2$, the basis can be transformed into $(A_\uparrow + \mathrm{i}A_\downarrow, B_\uparrow + \mathrm{i}B_\downarrow, A_\uparrow - \mathrm{i}A_\downarrow, B_\uparrow - \mathrm{i}B_\downarrow)^{\mathrm{T}}/\sqrt{2}$, wherein these two orthogonal mode types with hybridized layer degree of freedom serve as the effective 'pseudospin' degree of freedom. Meanwhile, the Hamiltonian can be decoupled into block-diagonal form through the unitary

transformation, yielding two independent spin subspaces:

$$H'(\mathbf{k}) = UH(\mathbf{k})U^{\dagger} = \begin{pmatrix} h_{\uparrow} & 0 \\ 0 & h_{\downarrow} \end{pmatrix}, \tag{2}$$

where $h_{\uparrow} = \begin{pmatrix} h_{13} & h_{12} \\ h_{12}^{*} & h_{24} \end{pmatrix}$ and $h_{\downarrow} = \begin{pmatrix} -h_{13} & h_{34} \\ h_{34}^{*} & -h_{24} \end{pmatrix}$ represent the spin-up and spin-down subspaces, respectively. Here, the terms h_{12} and h_{34} are graphenelike nearest-neighbor couplings within each layer, while h_{13} and h_{24} correspond to interlayer spin-orbit couplings between sublattices A and B, respectively. Notably, we explicitly exclude the Rashba spin-orbit coupling term in our model, as it would hybridize the spin-up and spin-down modes, leading to incomplete spin polarization in transport. The Hamiltonian $H'(\mathbf{k})$ is protected by time-reversal symmetry, satisfying $\mathcal{T}H'(\mathbf{k})\mathcal{T}^{-1} = H'(-\mathbf{k})$, where $\mathcal{T} = -\mathrm{i}\sigma_y \otimes \mathrm{I}_2\mathcal{K}$, with σ_y representing Pauli matrix and $\mathcal{K}$ representing complex conjugation operator.

The topological phase diagram of the system can be obtained by tuning the parameters t_{A} and t_{B}, as shown in Fig. 1(b). The triangular region formed by the red solid line (bottom right) and white central line carries the spin-Chern number $C_s = +1$, while its counterpart formed by the blue solid line (top left) and white central line exhibits $C_s = -1$. The green-colored first and third quadrants support antihelical edge states, while the yellow-colored second and fourth quadrants host helical edge states. Depending on the topological invariants and the existence of the bulk band that cross the Fermi level [46,47], the system exhibits a spin metal at point A (0.15, 0.15), spin-Chern metal at point B (0.225, 0.075), and spin-Chern semimetal at point C (0.225, 0). For the spin metal, there are no local gaps in the spin-polarized bands at K and K′ points, and its topology is characterized by the winding number instead of the spin Chern number. For the spin-Chern metal and spin-Chern semimetal, there exist locally spin-polarized band gaps at K and K′ points, and their topology is described by the spin-Chern number. The difference lies in that the bulk bands of the former cross the Fermi energy, while those of the latter are merely tangent to it. The details for topological invariants are provided in Supplemental Material [48].

Here, we focus on the spin metal at point A to exhibit the spin-dependent topological BICs with antihelical edge modes. The calculated bulk band structure along high-symmetry lines in the Brillouin zone is shown in Fig. 1(c). The red and blue bands correspond to the spin-up and spin-down subspaces, respectively. Remarkably, the pseudomagnetic flux induces opposite energy offsets at K and K′ points for opposite spins, leading to the Dirac points symmetrically traversing the Fermi level. This represents a hallmark signature of the topological spin metal. The calculated projected dispersions along the x direction with zigzag edges is shown in Fig. 1(d). The light red and blue regions correspond to the bulk-projected dispersions from the spin-up and spin-down subspaces, respectively. The solid lines depict the edge-state dispersions connecting the two Dirac points, which are doubly degenerate modes localized at opposite boundaries with identical group velocities (as indicated by their matching slopes) in each spin subspace. These results demonstrate the transport behavior of antihelical edge states, as demonstrated in Fig. 1(e). Crucially, the spin-up edge states (red lines) remain spatially localized while embedded within the spin-down bulk continuum, which is direct evidence of spin-dependent topological BICs. Analogously, the spin-down edge states (blue lines) are embedded within the spin-up bulk continuum without hybridization between them. Consequently, we have successfully exploited the decoupled nature of the two spin subspaces to realize spin-dependent topological BICs, which enable antihelical transport. Furthermore, edge states under bearded edge termination exhibit similar propagation characteristics, whereas armchair edge termination induces complete edge-state suppression due to bulk-cone hybridization at K and K′ points, as shown in Supplemental Material [48].

III. EXPERIMENT REALIZATION IN A PHONONIC CRYSTAL

Guided by the theoretical prediction, we consider a phononic crystal for implementation and observation of spin-dependent topological BICs. The sample was fabricated by 3D printing with photosensitive resin, as shown in Fig. 2(a). The sample features zigzag edge termination on both upper (edge-1) and lower (edge-2) edges. The hexagonal black dashed outline indicates a hexagonal unit cell, whose structural details are shown in Fig. 2(b). For clarity, only the air-filled regions are displayed, with the surrounding material acting as hard-wall boundary due to huge acoustic impedance mismatch compared with air. In mapping the phononic crystal to a tight-binding model, the red and blue cavities can be regarded as artificial atoms in sublattices A and B, respectively, while the straight tubes and staggered curved tubes provide intralayer and interlayer coupling terms, respectively. The hexagonal unit cell with a lattice constant $a = 65$ mm consists of cylindrical acoustic cavities with a radius of $r = 10$ mm and a height of $h = 45$ mm, which are stacked into a bilayer configuration with an interlayer spacing of 2 mm. These acoustic cavities are interconnected by straight intralayer tubes with a radius of 4.5 mm and curved interlayer tubes with a radius of 3 mm. The curved tubes connect to the lower cavities at a height of $3h/4$, and to the upper cavities at either $h/4$ (pale red tubes) for positive coupling or $3h/4$ (pale blue tubes) for negative coupling. This phononic crystal exhibits dipole modes near its central frequency of 3900 Hz, with intralayer and interlayer couplings measured as 85 Hz and 12.75 Hz, respectively. The simulated band structure of the unit cell is in excellent agreement with that derived from the tight-binding model (see the Supplemental Material [48] for the fitting results).

In our experimental setup, a balanced armature speaker is applied at upper resonator cavity to excite the sound field, while a microphone probe measures the acoustic signal within each resonator. The measured pressure fields from the top (p_1) and bottom (p_2) layers are combined into 'pseudospin' modes $p_{\pm} = p_1 \pm \mathrm{i}p_2$. By performing one-dimensional Fourier transform of the measured pressure at the cavities along the black dashed line in Fig. 2(a), we get the bulk-projected dispersions shown in Figs. 2(c) and 2(d), corresponding to the spin-up and spin-down subspaces, respectively. Throughout these measurements, open boundary conditions are maintained on both the left and right sides of the sample. The measured bulk-projected dispersions (color map) show great agreement with theoretical results (solid

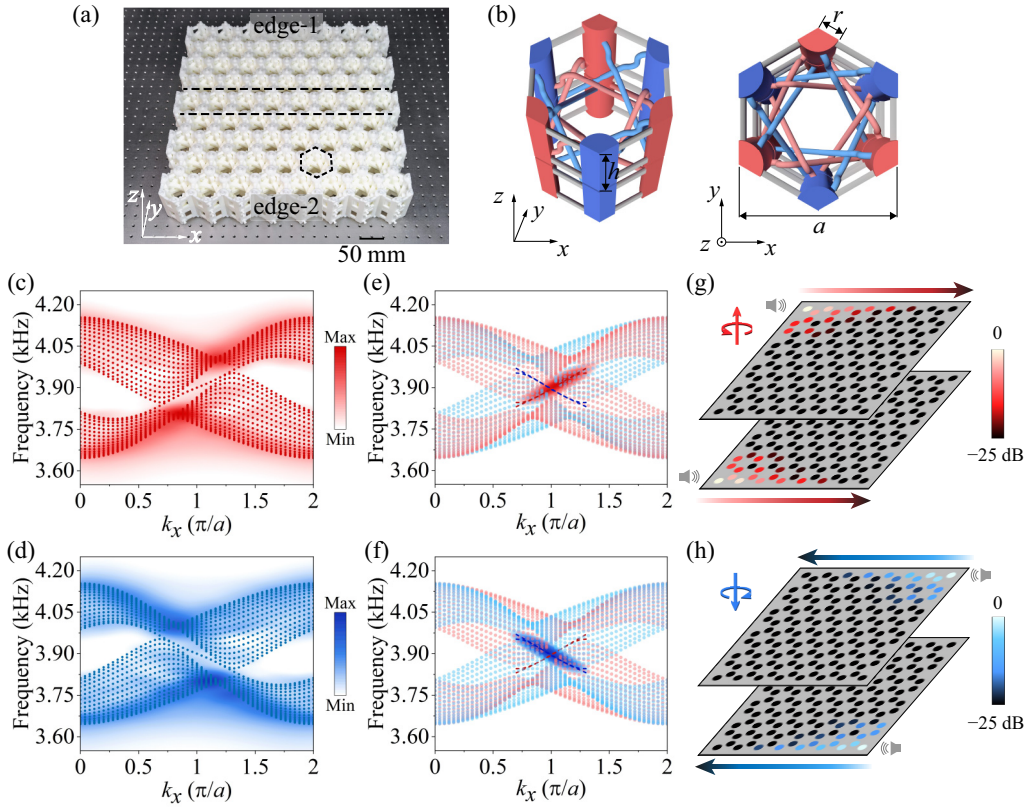

FIG. 2. Acoustic realization and measurement of spin-dependent topological BICs with antihelical transport. (a) Photograph of the phononic crystal sample, with a unit cell outlined by black dashed lines. (b) Unit cell structure with air-filled regions. Bulk-projected dispersions from the spin-up subspace (c) and spin-down subspace (d). The experimental results are represented by the color maps, while the calculated results, obtained under a central frequency of 3900 Hz and intralayer coupling of 85 Hz, are denoted by dots. Measured edge-state dispersions from the spin-up subspace (e) and spin-down subspace (f). Simulated dispersions (dashed lines) are overlaid on the experimental results (color map). Measured pressure field distributions of edge states at 3930 Hz from the spin-up subspace (g) and spin-down subspace (h).

dots), thereby providing the spin-dependent bulk mode spectrum required for constructing spin-dependent topological BICs.

We now present the experimental observation of antihelical edge states in topological BICs. The right- and left-propagating edge modes can be measured by placing the excitation source at the left and right side of the zigzag edge, respectively. After performing Fourier transform of the measured edge acoustic fields, we obtain the edge-state dispersions from the spin-up and spin-down subspaces, shown in the Figs. 2(e) and 2(f), respectively. They exhibit opposite group velocities but share the same spectral range of 3840–3960 Hz. The antihelical edge states from the spin-up subspace (red color map) are embedded within the continuum of extended bulk bands of the spin-down subspace (light blue dots). The measured acoustic pressure field distributions at 3930 Hz on the two zigzag edges are presented in Fig. 2(g). The spin-up acoustic fields exhibit strongly localized rightward propagation along two zigzag edges with rapid attenuation in the bulk. Owing to complete spin-subspace decoupling, they remain entirely unaffected by the spin-down bulk even embedded in the bulk modes. Notably, the edge-state propagation direction is spin-dependent, with spin-down edge states strictly forbidden from rightward propagation (see Supplemental Material for more details [48]). Correspondingly, Fig. 2(h) shows the measured spin-down pressure field distributions, exhibiting propagation characteristics exactly opposite to the spin-up case. The observation of antihelical edge propagation in Figs. 2(g) and 2(h) directly correspond to the theoretical predictions in Fig. 1(e). The above experimental results indicate the existence of the antihelical edge states embedded in the continuum spectrum of bulk states of another spin subspace.

We experimentally demonstrate independent modulation of the two topological BICs with different spins by tuning the sublattice-dependent interlayer coupling strengths. The interlayer coupling strengths t_A and t_B, which reflect the spin-orbit coupling strengths, govern the energy offsets at K and K′ points in the bulk bands. Simultaneously, the edge-state dispersions connect the conduction and valence bands of the same spin mode at K and K′ points, thereby providing a strategy for selectively controlling the propagation of the edge states. We tune the interlayer coupling to the spin-Chern metal phase, i.e., point B in Fig. 1(b). The simulated bulk band structure exhibits spin-polarized local gaps at K point in each subspace, as shown in Fig. 3(a). The difference of energy offset breaks the degeneracy of the edge-state dispersions, manifesting as distinct edge-state bandwidths and group

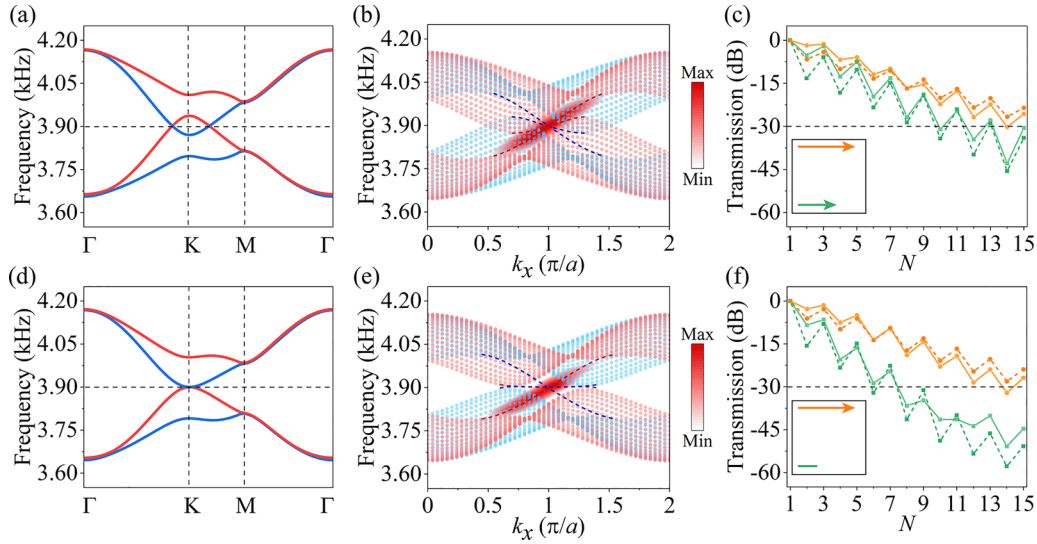

FIG. 3. The independent control of spin-dependent topological BICs. (a) Simulated bulk band of the spin-Chern metal at point B in Fig. 1(b). (b) Measured edge-state dispersion from spin-up subspace along the edge-1. Simulated dispersions (dashed lines) are overlaid on the experimental result (color map). (c) Edge-site field distributions at 3900 Hz. Speaker is applied at site $N = 1$, with orange (green) lines representing edge-1 (edge-2). (d)–(f) Same as (a)–(c), but for spin-Chern semimetal point C in Fig. 1(b). It exhibits a hybrid topological system, supporting the coexistence of the spin-dependent topological BICs and the flat bands.

velocities in Fig. 3(b). Due to the time-reversal symmetry of the two spin subspaces, we focus on the spin-up subspace as representative. The color map in Fig. 3(b) reveals the measured dispersion of the spin-up edge state along edge-1, which exhibits an extended frequency range (3800−4000 Hz) and a higher group velocity. Figure 3(c) displays the edge field distributions from both experiment (solid lines) and simulation (dashed lines), set to 0 dB at the speaker location ($N = 1$). Edge states propagating along the edge-2 (green) exhibit a modest suppression compared to those along edge-1 (orange). When the interlayer coupling is tuned to spin-Chern semimetal phase, i.e., point C in Fig. 1(b), the simulated bulk band structure is plotted in Fig. 3(d). The spin-up valence band and spin-down conduction band are tangent to the Fermi level at K point. As shown by the edge-state dispersions in Fig. 3(e), the system exhibits hybrid properties, where spin-dependent topological BICs coexist with topological flat bands. Notably, since the value of t_A at point C remains consistent with that at point B, their edge-1 dispersions share an identical group velocity and consequently exhibit nearly identical propagation properties, as shown in Figs. 3(c) and 3(f). The dispersionless nature of flatband suppresses edge-mode propagation along the edge-2, corresponding to the rapid field decay (green lines) in Fig. 3(f). These results demonstrate that by tuning the interlayer coupling strengths between sublattices, we can independently control the group velocity of antihelical edge transport in the topological BICs. This control capability gives rise to novel topological systems, such as a hybrid system with coexistence of spin-dependent BICs and topological flat bands, establishing a new paradigm for high-efficiency multimode hybrid transport. Furthermore, this system provides a platform for novel topological devices, as exemplified by the spin-dependent triangular signal splitter designed in Supplemental Material [48].

IV. CONCLUSIONS

In summary, we have theoretically proposed and experimentally observed spin-dependent topological BICs that support antihelical edge transport modes in a phononic crystal. The paradigm of spin-dependent topological BICs is enabled by the complete decoupling between spin-up and spin-down subspaces, which prevents hybridization of antihelical edge modes with bulk modes of the opposite subspace despite their spectral overlap. Through measurements of the projected dispersions and propagating field distributions, we confirm the existence of spin-dependent topological BICs. The antihelical edge states maintain localized transport along the zigzag edges even when embedded within the bulk continuum of the opposite spin. We further experimentally demonstrate that tuning the interlayer coupling strengths between sublattices enables independent control over the topological BICs with different spins, leading to some novel topological hybrid systems, such as a system with coexistence of spin-dependent BICs and topological flat bands. Our work not only deepens the understanding of topological BICs engineering via spin subspaces, but also opens new avenues for controllable hybrid multimode transport, paving the way for novel topological devices, such as spin-dependent signal splitter.

ACKNOWLEDGMENTS

This work was supported by the National Key Research and Development Program of China (No. 2022YFA1404501), the National Natural Science Foundation of China (No. 12304486, No. 12192253, No. 12474331, No. 12534014, and No. W2441005), and the Natural Science Foundation of Tianjin (No. 23JCQNJC01450).

DATA AVAILABILITY

The data that support the findings of this article are not publicly available upon publication because it is not technically feasible and/or the cost of preparing, depositing, and hosting the data would be prohibitive within the terms of this research project. The data are available from the authors upon reasonable request.

[1] J. von Neumann and E. P. Wigner, Über merkwürdige diskrete Eigenwerte, Phys. Z **30**, 465 (1929).

[2] C. W. Hsu, B. Zhen, A. D. Stone, J. D. Joannopoulos, and M. Soljačić, Bound states in the continuum, Nat. Rev. Mater. **1**, 16048 (2016).

[3] Y. Plotnik, O. Peleg, F. Dreisow, M. Heinrich, S. Nolte, A. Szameit, and M. Segev, Experimental observation of optical bound states in the continuum, Phys. Rev. Lett. **107**, 183901 (2011).

[4] N. Rivera, C. W. Hsu, B. Zhen, H. Buljan, J. D. Joannopoulos, and M. Soljačić, Controlling directionality and dimensionality of radiation by perturbing separable bound states in the continuum, Sci. Rep. **6**, 33394 (2016).

[5] D. C. Marinica, A. G. Borisov, and S. V. Shabanov, Bound states in the continuum in photonics, Phys. Rev. Lett. **100**, 183902 (2008).

[6] C. W. Hsu, B. Zhen, J. Lee, S.-L. Chua, S. G. Johnson, J. D. Joannopoulos, and M. Soljačić, Observation of trapped light within the radiation continuum, Nature (London) **499**, 188 (2013).

[7] S. Weimann, Y. Xu, R. Keil, A. E. Miroshnichenko, A. Tünnermann, S. Nolte, A. A. Sukhorukov, A. Szameit, and Y. S. Kivshar, Compact surface fano states embedded in the continuum of waveguide arrays, Phys. Rev. Lett. **111**, 240403 (2013).

[8] M. I. Molina, A. E. Miroshnichenko, and Y. S. Kivshar, Surface bound states in the continuum, Phys. Rev. Lett. **108**, 070401 (2012).

[9] G. Corrielli, G. Della Valle, A. Crespi, R. Osellame, and S. Longhi, Observation of surface states with algebraic localization, Phys. Rev. Lett. **111**, 220403 (2013).

[10] J.-H. Yang, Z.-T. Huang, D. N. Maksimov, P. S. Pankin, I. V. Timofeev, K.-B. Hong, H. Li, J.-W. Chen, C.-Y. Hsu, Y.-Y. Liu, T.-C. Lu, T.-R. Lin, C.-S. Yang, and K.-P. Chen, Low-threshold bound state in the continuum lasers in hybrid lattice resonance metasurfaces, Laser. Photon. Rev. **15**, 2100118 (2021).

[11] M.-S. Hwang, K.-Y. Jeong, J.-P. So, K.-H. Kim, and H.-G. Park, Nanophotonic nonlinear and laser devices exploiting bound states in the continuum, Commun. Phys. **5**, 106 (2022).

[12] M.-S. Hwang, H.-C. Lee, K.-H. Kim, K.-Y. Jeong, S.-H. Kwon, K. Koshelev, Y. Kivshar, and H.-G. Park, Ultralow-threshold laser using super-bound states in the continuum, Nat. Commun. **12**, 4135 (2021).

[13] A. A. Lyapina, D. N. Maksimov, A. S. Pilipchuk, and A. F. Sadreev, Bound states in the continuum in open acoustic resonators, J. Fluid Mech. **780**, 370 (2015).

[14] L. Huang, Y. K. Chiang, S. Huang, C. Shen, F. Deng, Y. Cheng, B. Jia, Y. Li, D. A. Powell, and A. E. Miroshnichenko, Sound trapping in an open resonator, Nat. Commun. **12**, 4819 (2021).

[15] S. Huang, T. Liu, Z. Zhou, X. Wang, J. Zhu, and Y. Li, Extreme sound confinement from quasibound states in the continuum, Phys. Rev. Appl. **14**, 021001(R) (2020).

[16] I. Deriy, I. Toftul, M. Petrov, and A. Bogdanov, Bound states in the continuum in compact acoustic resonators, Phys. Rev. Lett. **128**, 084301 (2022).

[17] L. Huang, S. Huang, C. Shen, S. Yves, A. S. Pilipchuk, X. Ni, S. Kim, Y. K. Chiang, D. A. Powell, J. Zhu, Y. Cheng, Y. Li, A. F. Sadreev, A. Alù, and A. E. Miroshnichenko, Acoustic resonances in non-Hermitian open systems, Nat. Rev. Phys. **6**, 11 (2023).

[18] M. McIver, An example of non-uniqueness in the two-dimensional linear water wave problem, J. Fluid Mech. **315**, 257 (1996).

[19] C. Linton and P. McIver, Embedded trapped modes in water waves and acoustics, Wave Motion **45**, 16 (2007).

[20] X. Fan and I. M. White, Optofluidic microsystems for chemical and biological analysis, Nat. Photon. **5**, 591 (2011).

[21] M. Z. Hasan and C. L. Kane, *Colloquium*: Topological insulators, Rev. Mod. Phys. **82**, 3045 (2010).

[22] X.-L. Qi and S.-C. Zhang, Topological insulators and superconductors, Rev. Mod. Phys. **83**, 1057 (2011).

[23] W. Zhu, W. Deng, Y. Liu, J. Lu, H.-X. Wang, Z.-K. Lin, X. Huang, J.-H. Jiang, and Z. Liu, Topological phononic metamaterials, Rep. Prog. Phys. **86**, 106501 (2023).

[24] K. v. Klitzing, G. Dorda, and M. Pepper, New method for high-accuracy determination of the fine-structure constant based on quantized Hall resistance, Phys. Rev. Lett. **45**, 494 (1980).

[25] C. L. Kane and E. J. Mele, Quantum spin Hall effect in graphene, Phys. Rev. Lett. **95**, 226801 (2005).

[26] C. L. Kane and E. J. Mele, Z_2 topological order and the quantum spin Hall effect, Phys. Rev. Lett. **95**, 146802 (2005).

[27] B. A. Bernevig, T. L. Hughes, and S.-C. Zhang, Quantum spin Hall effect and topological phase transition in HgTe quantum wells, Science **314**, 1757 (2006).

[28] X.-L. Qi and S.-C. Zhang, The quantum spin Hall effect and topological insulators, Phys. Today **63**(1), 33 (2010).

[29] W. Deng, X. Huang, J. Lu, V. Peri, F. Li, S. D. Huber, and Z. Liu, Acoustic spin-Chern insulator induced by synthetic spin–orbit coupling with spin conservation breaking, Nat. Commun. **11**, 3227 (2020).

[30] J. Wu, R. Zheng, J. Liang, M. Ke, J. Lu, W. Deng, X. Huang, and Z. Liu, Spin-dependent localization of helical edge states in a non-Hermitian phononic crystal, Phys. Rev. Lett. **133**, 126601 (2024).

[31] L. Xie, L. Jin, and Z. Song, Antihelical edge states in two-dimensional photonic topological metals, Sci. Bull. **68**, 255 (2023).

[32] Y.-M. Li, Antihelical edge magnons in patterned antiferromagnetic thin films, Phys. Rev. Res. **5**, 033026 (2023).

[33] L. Liu, C.-M. Miao, Q.-F. Sun, and Y.-T. Zhang, Two-dimensional higher-order topological metals, Phys. Rev. B **110**, 205415 (2024).

[34] X. Dai, P.-H. Fu, Y. S. Ang, and Q. Chen, Two-dimensional Weyl nodal-line semimetal and antihelical edge states in a modified Kane-Mele model, Phys. Rev. B **110**, 195409 (2024).

[35] T. Xia, Q. Zhang, and C. Qiu, Observation of antihelical edge states in acoustic metamaterials, Phys. Rev. Lett. **135**, 056601 (2025).

[36] Y.-X. Xiao, G. Ma, Z.-Q. Zhang, and C. T. Chan, Topological subspace-induced bound state in the continuum, Phys. Rev. Lett. **118**, 166803 (2017).

[37] X. Wang, D. Bongiovanni, Z. Wang, A. Abdrabou, Z. Hu, D. Jukić, D. Song, R. Morandotti, R. El-Ganainy, Z. Chen, and H. Buljan, Construction of topological bound states in the continuum via subsymmetry, ACS Photonics **11**, 3213 (2024).

[38] R. Dong, Y. Zhu, D. Mao, X. Wang, and Y. Li, Observation of extreme anisotropic sensitivity at topological bound states in the continuum, Phys. Rev. Lett. **134**, 206601 (2025).

[39] L. Liu, T. Li, Q. Zhang, M. Xiao, and C. Qiu, Universal mirror-stacking approach for constructing topological bound states in the continuum, Phys. Rev. Lett. **130**, 106301 (2023).

[40] X.-Y. Liu, Y. Liu, Z. Xiong, H.-X. Wang, and J.-H. Jiang, Higher-order topological phases in bilayer phononic crystals and topological bound states in the continuum, Phys. Rev. B **109**, 205137 (2024).

[41] J. Guo, Z. Gu, and J. Zhu, Realization of merged topological corner states in the continuum in acoustic crystals, Phys. Rev. Lett. **133**, 236603 (2024).

[42] Z. Pu, H. He, L. Luo, Q. Ma, L. Ye, M. Ke, and Z. Liu, Acoustic higher-order Weyl semimetal with bound hinge states in the continuum, Phys. Rev. Lett. **130**, 116103 (2023).

[43] S. Yin, L. Ye, H. He, X. Huang, M. Ke, W. Deng, J. Lu, and Z. Liu, Valley edge states as bound states in the continuum, Sci. Bull. **69**, 1660 (2024).

[44] S. Yin, Z. Wang, L. Ye, H. He, M. Ke, W. Deng, J. Lu, and Z. Liu, Dimensional hierarchy of topological bound states in the continuum, Phys. Rev. Lett. **135**, 126602 (2025).

[45] L. Qian, W. Zhang, H. Sun, and X. Zhang, Non-Abelian topological bound states in the continuum, Phys. Rev. Lett. **132**, 046601 (2024).

[46] Y.-C. Zhou, Z.-Q. Sun, H.-S. Lai, X.-C. Sun, C. He, and Y.-F. Chen, Observation of photonic Chern metal with bichiral edge propagation, Laser Photon. Rev. **18**, 2400826 (2024).

[47] J. Chen, Y. Zheng, S. Yang, A. Alù, Z.-Y. Li, and C.-W. Qiu, Chern-protected flatband edge state in metaphotonics, Phys. Rev. Lett. **134**, 223806 (2025).

[48] See Supplemental Material at http://link.aps.org/supplemental/10.1103/gmbp-csmg for the topological invariants; projected dispersions for bearded edges and armchair edges; numerical simulations and the agreement between acoustic structure and tight-binding model; and the unidirectional propagation of spin-dependent edge states.